Combination of Independent Vector Analysis and Improved Fast Independent Component Analysis for Speckle Noise Reduction in Synthetic Aperture Radar Images

Xianglei Liu,[1] Yutong Wang,[1] Runjie Wang,[1,2*] and Nilufar Adil[1]

[1]Key Laboratory for Urban Geomatics of National Administration of Surveying, School of Geomatics and Urban Spatial Informatics, Beijing University of Civil Engineering and Architecture, Zhanlanguan Road, Beijing 100048, PR China
[2]Beijing Key Laboratory of Urban Spatial Information Engineering, No.15 Yangfangdian Road, Beijing 100038, PR China

The coherent properties of radar give rise to speckle noise in synthetic aperture radar (SAR) images. Speckle noise, mixed with valid information, directly affects information extraction in SAR images, especially the accuracy of persistent scatter point selection. Based on a detailed analysis of speckle noise characteristics, an innovative speckle noise reduction method combining independent vector analysis and an improved fast independent component analysis (FastICA) is proposed in this study. First, the principle of independent vector separation is followed to retain the maximum correlation of internal information in each channel of the SAR image. Then, a high-order Newton iterative scheme is constructed and added to the traditional FastICA algorithm to improve the speed and stability of iteration processing. Finally, the relaxation factor is introduced to relax the initial value requirement to minimize image distortion during speckle noise reduction. To verify the proposed algorithm, two groups of SAR images are selected from "Sandia National Laboratories" and Sentinel-1A. The proposed algorithm is compared with several other algorithms on speckle noise reduction efficiency. The experimental results showed that the proposed method could more effectively reduce speckle noise and retain edge features of SAR images, indicating that it had a potential to enhance image quality for the subsequent interpretation of SAR images.

1. Introduction

Synthetic aperture radar (SAR) is a sophisticated sensor technology used for remote sensing using active microwave technology.[1] It has all-day, all-weather observation ability as well as a certain penetration mode.[2] However, in a SAR imaging system, all the scatters' distribution positions in the resolution unit are always disparate from their accumulated energy.[3] This

---

discrepancy causes the gray values of adjacent pixels to fluctuate around the average value. Speckle noise then appears. It is usually intertwined with a valid signal. This will lead to pixel misjudgment and feature calibration errors, which will affect the accuracy of target recognition and classification.[4] Hence, it is imperative and crucial to mitigate the speckle noise prior to SAR image analysis.[5]

In SAR imagery, the standard deviation of speckle noise is directly proportional to the signal intensity, leading to a multiplicative speckle noise model.[6] To eliminate the speckle noise, numerous despeckling approaches have been developed and widely used, including the enhanced Sigma, Kuan, Lee filtering, and nonlocal means despeckling methods.[7] They are easy to implement but limited in their adaptability.[8] Transformation-domain-based algorithms exhibit excellent performance in terms of adaptability, but there are challenges in phase accuracy and detail retention. Therefore, researchers turn to model-based optimization techniques such as probabilistic patch basis (PPB) and nonlocal low-rank (NLLR) algorithms, as well as block-matching and 3D filtering (BM3D) algorithm that combines spatial and transform domains.[9] Although they can retain details, they have high requirements for phase accuracy and high computational complexity.[10–12] Moreover, these algorithms usually process multiple channels of SAR image data together in the process of despeckling, which leads to ignoring correlation between channels and dependence within channels.

From the imaging principle of SAR, the presence of speckle noise caused by interference from various backscattering paths is intricately linked to the inherent scattering characteristics within the image.[13] To avoid the occurrence of the above method problem, researchers have developed the fast independent component analysis (FastICA) algorithm and the independent vector analysis (IVA) method. Each SAR image contains a large number of pixels and is usually presented as a complex representation of the radar scattering coefficient, which makes the despeckling processing very slow.[14] After continuous improvement, FastICA is widely used in image speckle removal because of its rapid convergence. However, when dealing with large-scale data such as SAR data with complex statistical distribution, operational efficiency will also be decreased. Additionally, if the choices of step size and initial value are not suitable, it will lead to image distortion.[15] Besides, the FastICA algorithm usually assumes that components are linearly independent of each other, which may not be appropriate for some complex mixing cases.[16] Moreover, FastICA tends to overlook correlation between specific channels and pixel values in SAR image data, resulting in a smooth transition and potential distortion when generating despeckling image. IVA can alleviate the problems existing in the traditional FastICA method. In IVA, all frequency components are treated as a stochastic vector variable and processed simultaneously, and datasets with correlations are preserved by separating dependences across samples within the dataset. It can represent pixel values in channels as vectors and retain correlation information to avoid edge loss or excessive smoothing.[17]

Thus, to enhance the effectiveness of speckle noise reduction in SAR images, an innovative speckle noise reduction method combining IVA and an improved FastICA is proposed in this study. The method can minimize excessive smoothing and distortion during image noise reduction. It can also preserve correlations between different SAR data sources. In this study, we also conduct an experimental analysis based on the speckle distribution characteristics of SAR

images and their power spectral density function (PSD) modeling. Moreover, to evaluate the effectiveness of the proposed method, experiments are conducted using both simulated and real data. The following sections of this paper are structured as follows. In Sect. 2, the integrated methodology flow and an explanation of its key components are provided. Comparative experiments and performance evaluation of the method are presented in Sect. 3. Finally, the summary of the main findings and suggestion for future research directions can be found in Sect. 4.

2.   Methods

In general, SAR images are usually generated by multi-look processing to reduce random noise. However, speckle noise is an inherent property caused by the coherent reflection of ground targets, so it needs special treatment. Existing noise reduction methods face challenges in maintaining relevance and computational efficiency. The algorithm proposed in this paper aims to alleviate these problems efficiently, and in this section, we describe in detail its method principle and process. Figure 1 shows the entire workflow of the proposed speckle noise reduction algorithm for SAR images, including the following three key technologies: (1) multiplicative speckle noise model construction, (2) effective preservation within the single channel pixel's correlation and reduction of edge loss or excessive smoothing using the IVA principle, and (3) distortion avoidance and efficiency improvement based on the improved FastICA method.

2.1   Multiplicative speckle noise model construction

Every pixel in a SAR image results from the backscattered wave of a large number of point scatters located in one resolution cell, which can be modeled as a complex value.[18] This representation includes both the magnitude and phase information of the scattering intensity, which is crucial for characterizing spatial structure and motion properties. However, processing complex numbers increases computational complexity, resulting in reduced computing speed during despeckling processes, especially with large-scale datasets. It is represented as

$$Ae^{j\varphi} = \sum_{i=1}^{R} A_i e^{j\varphi_i},$$ (1)

where A_i and $e^{j\varphi_i}$ are the individual amplitude and phase of the backscattering, respectively, and R is the total number of scatters within the resolution cell. As A_i and φ_i are unobservable because the individual scatters are much smaller than the resolution cell, the speckle can be formulated as a multiplicative model of pixel anomaly:

$$O = I \cdot Y,$$ (2)

where O is the observation result, I is the average backscattered intensity, and Y is the noise
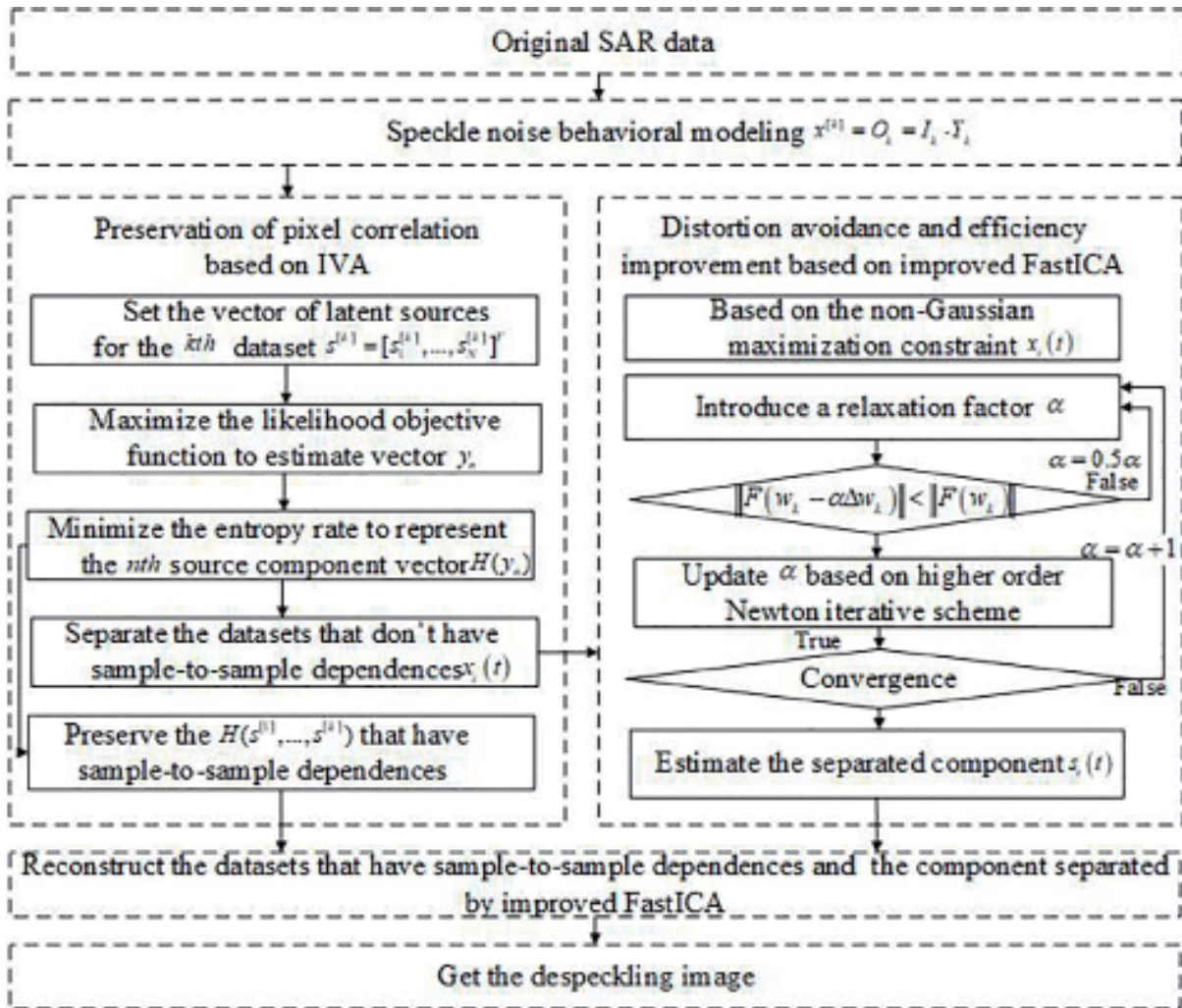
Fig. 1. Workflow of the proposed algorithm for speckle noise reduction.

intensity. I and Y are considered constants and independent random variables. Owing to the scattering characteristics of SAR, each channel of SAR data usually represents a specific observation or polarization mode.[19] If the SAR imagery is multi-channel, the Kth channel information O_K as well as $\boldsymbol{x}^{[K]}$, $K = 1, ..., M$ in observed data can be linked to the speckle noise modeling with the following transformation:

$$\boldsymbol{x}^{[K]} = O_K = I_K \cdot Y_K, \tag{3}$$

where I_K and Y_K correspond to the true backscattered intensity reflectivity and speckle noise, respectively.

Each pixel value within the channel represents information of different directions or polarizations over the same time or space, which are correlated.[20] Previous algorithms usually do not take this correlation into account, while IVA can preserve the correlation when dealing

with linearity and nonlinearity in the data.[21] Therefore, in Sect. 2.2, how to preserve the correlation based on IVA is described.

2.2 Data sources' correlation preservation in SAR image based on IVA principle

To preserve the correlation, the pixel values of each channel of SAR images are first represented as multiple datasets. Subsequently, sources exhibiting sample-to-sample dependences are separated and preserved within these datasets. This process is governed by the objective function and ensures the preservation of the internal correlation specific to each SAR data channel.

2.2.1 SAR channel dataset setting

Since it is specified that the SAR image resolution unit has at least two pixels, the identity matrix of $m \times n$ ($m = 2$, $n = 2$) dimensions is set as the initial value of the dataset range in this study. According to Ref. 22, it is determined whether the dataset meets the IVA decomposition conditions, and to adjust $m = m + 1$, $n = n + 1$ until it does.[22] The key steps involved in IVA decomposition are as follows:

$$x^{[K]} = B^{[K]} s^{[K]}, K = 1, ..., M, \tag{4}$$

where the vector of latent sources for the Kth dataset $s^{[K]} = [s_1^{[K]}, ..., s_N^{[K]}]^T$ represents a linear combination of a total of N statistically independent sources. To estimate M demixing matrices $B^{[K]}$ ($B^{[K]} \in \mathbb{R}^{N \times N}$) and yield source estimates $y^{[K]} = W^{[K]} x^{[K]}$, the nth source from each of the M datasets is vertically concatenated and denoted as

$$s_n = [s_n^{[1]}, ..., s_n^{[M]}]^T, \tag{5}$$

where s_n is a vector with M dimensions. The optimization parameter consists of a set of demixing matrices $W^{[1]}$, ..., $W^{[M]}$, which can be organized into a 3D array $w \in \mathbb{R}^{N \times N \times M}$. Upon establishing the dataset configuration, the IVA algorithm seeks to optimize the demixing process through objective functions that maximize the statistical independence of the separated sources.[23] In this process, the maximum likelihood (ML) function and the mutual information (MI) function are crucial when separating the observed data $x^{[K]}$ into its constituent sources $s^{[K]}$.[24]

2.2.2. Data sources' reservation with sample-to-sample dependences based on IVA objective functions

ML and MI are more suitable for the SAR image processing task in this study than other potential objective functions such as squared error minimization and cross-entropy minimization because they can better take into account the statistical properties and nonlinear characteristics of the image. The objective function of IVA can be defined as maximizing the logarithm of the

likelihood in its natural form.[25] The objective function ML is calculated as

$$J_{IVA}(\boldsymbol{w}) = \sum_{n=1}^{N} E\left\{\log p(\boldsymbol{y}_n)\right\} + \sum_{K=1}^{M} \log\left|\det(\boldsymbol{W})^{[K]}\right|, \tag{6}$$

where $\det(\boldsymbol{W})^{[K]}$ is the determinant of the matrix $\boldsymbol{W}^{[K]}$, $\boldsymbol{y}_n$ is the nth estimated vector, and $p(\boldsymbol{y}_n)$ is its multidimensional probability density function (PDF).

Similarly, the MI objective function for the IVA model is determined by

$$J_{IVA}(\boldsymbol{w}) = \sum_{K=1}^{N} H(\boldsymbol{y}_n) - \sum_{K=1}^{M} \log\left|\det(\boldsymbol{W}^{[K]})\right| - H\left(\boldsymbol{x}^{[1]},...,\boldsymbol{x}^{[K]}\right), \tag{7}$$

where the entropy of the nth source component vector (SCV) is represented by $H(\boldsymbol{y}_n)$ considering $H(\boldsymbol{x}^{[1]},...,\boldsymbol{x}^{[K]})$ as a constant factor. This frame can be morphed as

$$J_{IVA}(\boldsymbol{w}) = \sum_{n=1}^{N} \left(\sum_{K=1}^{M} H\left(\boldsymbol{y}_n^K\right) - I(\boldsymbol{y}_n) \right) - \sum_{K=1}^{M} \log\left|\det(\boldsymbol{W}^{[K]})\right| - H\left(\boldsymbol{x}^{[1]},...,\boldsymbol{x}^{[M]}\right), \tag{8}$$

where the term $I(\boldsymbol{y}_n)$ presents the measure of shared information within the nth SCV. We can observe that the entropy rate of the estimated SCVs is minimized by IVA. Finally, we can obtain the demixing matrices and yield $\boldsymbol{y}_n$. Without the mutual information term, the objective function is equivalent to performing independent ICA separately on each dataset.[26] Therefore, the next key step in this study is to use the improved FastICA algorithm to despeckle the datasets that do not have sample-to-sample dependences $\boldsymbol{x}^{\prime[K]}$.

2.3   Distortion avoidance and efficiency improvement based on improved FastICA

After the above retention of sources with the datasets that have sample-to-sample dependences, the improved FastICA algorithm is applied to the datasets that do not have sample-to-sample dependences to realize speckle noise suppression. The higher the iteration order, the more sensitive it is to the initial value.[27] Therefore, the adaptive updating of the convergence factor in this study expands the selection range of the initial value to achieve distortion avoidance. The details are shown in Sects. 2.3.1 and 2.3.2.

2.3.1   High-order Newton iterative scheme for efficiency improvement

Negative entropy is chosen to measure the non-Gaussian separated signals.[28] If the negative entropy reaches a maximum, it is considered that each independent pixel value has been successfully extracted from the datasets $\boldsymbol{x}^{\prime[K]}$ that do not have sample-to-sample dependences. By taking the extreme value of $E\{G(\boldsymbol{w}^{\prime T}\boldsymbol{x}^\prime)\}$, we can obtain the basic formula of FastICA as follows. The constraint is

$$E\left\{\left((\boldsymbol{w}')^{T} \boldsymbol{x}'\right)^{2}\right\} = \|\boldsymbol{w}'\|^{2} = 1, \tag{9}$$

where E usually stands for expectation and w' stands for the weight or separation matrix. Finally, it can be derived as

$$E\left\{\boldsymbol{x}'\boldsymbol{x}'^{T} g'\left((\boldsymbol{w}')^{T} \boldsymbol{x}'\right)\right\} \approx E\left\{\boldsymbol{x}'(\boldsymbol{x}')^{T}\right\} E\left\{g'\left((\boldsymbol{w}')^{T} \boldsymbol{x}'\right)\right\} = E\left\{g'\left((\boldsymbol{w}')^{T} \boldsymbol{x}'\right)\right\} \boldsymbol{I}, \tag{10}$$

where g is a nonlinear function to estimate non-Gaussian properties and stands for the identity matrix. At each iteration, we increase the independence of the signal by adjusting the weight vector until a predetermined convergence standard is reached. According to Ref. 28, the above equation can be further simplified and replaced by the following iterative approximate solution:

$$\boldsymbol{w}'_{k+1} = \frac{\boldsymbol{w}'_{k} - \left[E\left\{\boldsymbol{x}'g\left((\boldsymbol{w}')^{T} \boldsymbol{x}'\right)'\right\} - \beta\boldsymbol{w}'_{k}\right]}{\left[E\left\{g'\left((\boldsymbol{w}')^{T} \boldsymbol{x}'\right)\right\} - \beta\right]}, \tag{11}$$

where the $(k + 1)$th iteration process is part of the traditional FastICA for the separation matrix w' in the second-order Newton iterative format. β is a parameter related to the step size.

On the basis of the established theoretical framework, we adopt the Newton iteration scheme in this study to update the step size. The Newton iterative method with a second-order convergence rate is given by

$$\boldsymbol{x}'_{q+1} = \boldsymbol{x}'_{q} - \frac{f(\boldsymbol{x}'_{q})}{f'(\boldsymbol{x}'_{q})}; \tag{12}$$

the high-order convergence Newton point substitution method is obtained by using the correlation analysis and transformation of the Newton iterative formula. Thus, it has a higher convergence speed.[29] The Newton iterative method is modified to obtain

$$\boldsymbol{x}^{*}_{q+1} = \boldsymbol{x}_{q} - \frac{f(\boldsymbol{x}_{q})}{\lambda f'(\boldsymbol{x}_{q})}, \tag{13}$$

where $q = 0, 1, 2, ..., k$. According to Ref. 30, the modified Newton iterative algorithm has at least a third-order convergence speed. By adjusting the value, it can achieve a higher accuracy. The third-order convergence formula of FastICA can be deduced successively as

$$\begin{cases} \boldsymbol{w}^1 = E\left\{\boldsymbol{x}'g\left((\boldsymbol{w}')^T \boldsymbol{x}'\right)\right\} - 2E\{g'\left((\boldsymbol{w}')^T \boldsymbol{x}'\right)\}\boldsymbol{w}' \\ \boldsymbol{w}^2 = E\left\{\boldsymbol{x}'g\left(\boldsymbol{w}^T \boldsymbol{x}'\right)\right\} - E\{g'\left((\boldsymbol{w}^1)^T \boldsymbol{x}'\right)\}\boldsymbol{w}' \\ \boldsymbol{w}^\# = \dfrac{\boldsymbol{w}'^2}{\|\boldsymbol{w}'^2\|} \end{cases}, \tag{14}$$

and the high-order Newton iterative scheme can enhance the convergence efficiency of the algorithm when applied. However, the orthogonalization process of the solution vector relies on utilizing the previous solution vector as the subsequent initial value. Consequently, high-order iterations are more susceptible to variations in initial value, thereby impacting the ultimate convergence outcome resulting in the distortion of the image.

2.3.2 Relaxation factor introduced for initial value selection

To avoid distortion to the greatest extent, it is necessary to relax the range of the initial value to achieve a large range of convergence. To improve the algorithm's requirement for the initial value $\boldsymbol{w}_0$, the relaxation factor α is introduced into the iterative formula:

$$\boldsymbol{w}'_{k+1} = \alpha E\left\{\boldsymbol{x}'g\left((\boldsymbol{w}'_k)^T \boldsymbol{x}\right)\right\} - E\left\{g'\left((\boldsymbol{w}'_k)^T \boldsymbol{x}'\right)\right\}\boldsymbol{w}'_k - (1-\alpha)\beta\boldsymbol{w}'_k. \tag{15}$$

The reason for choosing α is that it needs to be satisfied under a certain paradigm:

$$\left\|E\left\{\boldsymbol{x}'g\left((\boldsymbol{w}'_{k+1})^T \boldsymbol{x}'\right)\right\} - \beta(\boldsymbol{w}'_{k+1})^T\right\| \lessdot \left\|E\left\{\boldsymbol{x}'g\left((\boldsymbol{w}'_k)^T \boldsymbol{x}'\right)\right\} - \beta(\boldsymbol{w}'_k)^T\right\|. \tag{16}$$

That is, by introducing α, we can guarantee the descending property of the value of the objective function. according to $F(\boldsymbol{w}_k)$. This descending property for consistency can force the Newton iterative method to enter the convergence region from a certain point $\boldsymbol{w}'_k$, enabling the algorithm to achieve convergence in any case. Set $\alpha = 1$ (i.e., the traditional FastICA algorithm) and then calculate Δw_k and check whether the following constraint conditions have been satisfied:

$$\min\left\|F\left(\frac{\boldsymbol{w}_k - \alpha F(\boldsymbol{w}_k)}{JF(\boldsymbol{w}_k)}\right)\right\|, \tag{17}$$

where $F(\boldsymbol{w}_k)$ is the objective function that represents a measure of non-Gauss and J denotes the Jacobian matrix about $F(\boldsymbol{w}_k)$. The Jacobian matrix is used to describe the first-order change of the objective function near the weight vector in the algorithm and contains all the partial derivative information of the function at the current point gradient. It is the key to update the weight and evaluate the convergence in the iterative process. If the above constraint is not

satisfied, set $\alpha = 0.5\alpha$, because a smaller α value can enhance the stability of the algorithm and prevent iteration divergence caused by too large a step length. If the despeckling quality evaluation index value is not meeting the expectations, set $\alpha = \alpha + 1$. As shown in Fig. 1, the steps will be repeatedly performed until the condition is satisfied. Finally, the improved FastICA algorithm iteration is completed.

3.   Experimental Results

To evaluate the efficiency of the proposed method, two experiments using both simulative generated speckled images and real SAR images are conducted. The proposed approach is compared against existing methods including PPB, BM3D, NLLR, LEE, and KUAN. To further compare its performance, the despeckling results using the equivalent number of looks (ENL), efficient perceptual image (EPI), mean absolute error (MAE), peak signal-to-noise ratio (PSNR), structural similarity index measure (SSIM), coefficient of variation (CV), mean of ratio (MoR), and central processing unit (CPU) time are demonstrated.[31,32] The best performance is achieved by fine-tuning the parameters in all of these algorithms. For PPB, we used a patch size of 5 × 5 pixels with an 8 × 8 search window. The BM3D algorithm is configured with a hard thresholding block matching parameter of 2500 and a Wiener filter for the final estimate. The NLLR utilized a search window of 10×10 pixels with a similarity threshold of 0.1. The LEE filter is tuned with a 7 × 7 window size, using local statistics to estimate the noise variance. Lastly, the KUAN filter operated with a 3 × 3 kernel, applying a local minimum mean square error approach. These images are subjected to normalization and assumed to be confined within their lower and upper limits, specifically in the range from 0 to 1. These settings are determined after multiple preliminary runs to balance the trade-off between noise suppression and detail preservation. These experiments are conducted using Python version 3-V on a computer equipped with an Intel (CITM) i7-6700 CPU running at a speed of 3.40 GHz (with a boost frequency of 3.41 GHz), accompanied by 8 GB of RAM and operating on a 64-bit system.

3.1   Simulation experiment and result analysis

To evaluate the efficiency of the method proposed in this study, a simulation experiment on SAR image speckle noise reduction is first performed. The simulation experimental image sources are from "Sandia National Laboratories", whose website SAR images had no notable speckle noise.[33] These images are utilized as reference images to assess performance. Figure 2(a) shows the image of the Jacksonville Naval Air Station region captured through the SpotDwell mode in the Ku-band, referred to as 'Building' [600 × 600]. Figure 2(c) showcases an image of a dirt road access gate at Kirtland AFB in the Ka-band, named 'Road' [411 × 411]. To simulate SAR image embedded speckle noise, we multiplied simulated speckle with noise-free synthetic images in amplitude format following Dellepiane's method from 2011, as shown in Figs. 2(b) and 2(d).[34] The results of PSD function modeling for embedded speckles within the reference image are presented in Fig. 3. Table 1 illustrates the PSD results based on their peak
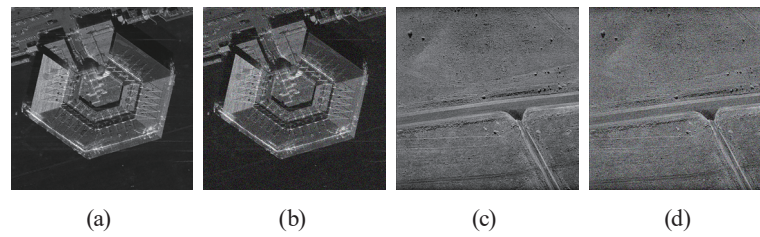
Fig. 2.   Synthetic images used in simulation: (a) building, (b) synthetically speckled noisy building, (c) road, and (b) synthetically speckled noisy road.
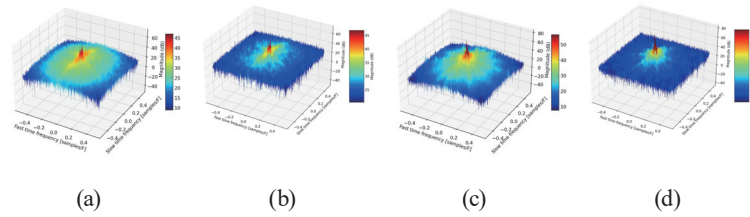

Fig. 3.   (Color online) PSD modeling of synthetic images: (a) PSD of building, (b) PSD of synthetically speckled noisy building, (c) PSD of road, and (d) PSD of synthetically speckled noisy road.

Table 1
PSD modeling results before speckle noise suppression.

Images	Preprocessed	Value (dB)
Building	Original	22
	Speckled	28.07
Road	Original	22.7
	Speckled	26.29

values of different images before undergoing speckle noise reduction. Some studies indicate that effective despeckling in SAR images is indicated by a PSD model with few but uniformly intense peaks. This means that good noise reduction is achieved when the PSD shows a small number of strong peaks rather than a lot of scattered ones.

The comparative analysis of speckle noise reduction is performed using six methods, with results illustrated in Figs. 4 and 6, and PSD outcomes depicted in Figs. 5 and 7. Visually, NLLR and PPB left notable noise shown in Figs. 4(d) and 4(e), as well as in Figs. 6(d) and 6(e), while KUAN and LEE resulted in blurred edges shown in Figs. 4(b) and 4(c), as well as in Figs. 6(b) and 6(c). Besides, minor artifacts are observed using these conventional methods. The proposed method maintained details with minimal artifacts, demonstrating superior speckle reduction and detail preservation performance.

To conduct a quantitative metrics evaluation, the corresponding PSD outcomes are depicted in Figs. 5 and 7. Table 2 shows the respective peak values of these different PSD outcomes. The PSDs after applying despeckling methods generally show a reduced peak height compared with the noisy image, suggesting effective speckle noise reduction. Among this despeckling methods,
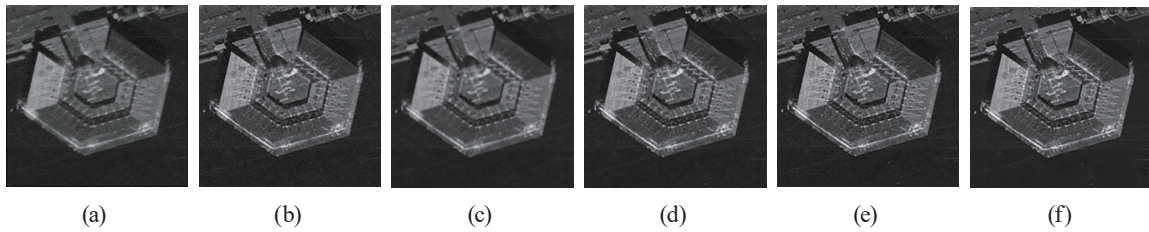
(a)　　　　(b)　　　　(c)　　　　(d)　　　　(e)　　　　(f)

Fig. 4. Despeckling results in building image using (a) BM3D, (b) KUAN, (c) LEE, (d) NLLR, (e) PPB, and (f) proposed methods.

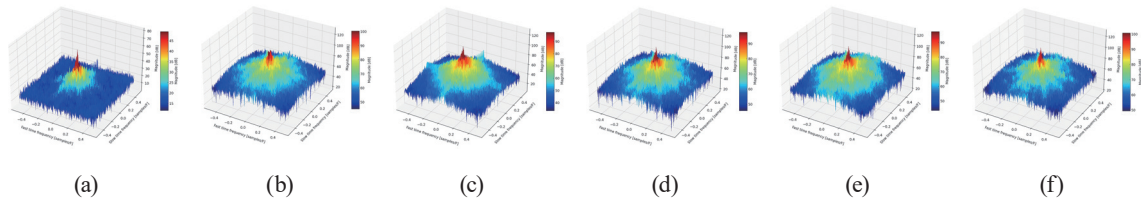(a)　　　　(b)　　　　(c)　　　　(d)　　　　(e)　　　　(f)

Fig. 5. (Color online) PSD modeling of despeckling resulst in building image under (a) BM3D, (b) KUAN, (c) LEE, (d) NLLR, (e) PPB, and (f) proposed methods.
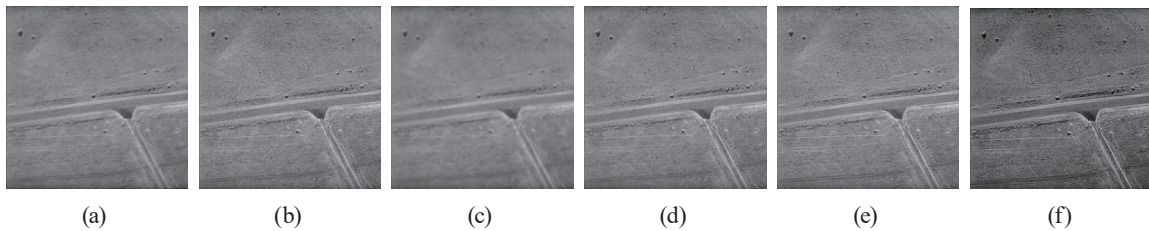

(a)　　　　(b)　　　　(c)　　　　(d)　　　　(e)　　　　(f)

Fig. 6. Despeckling results in road image using (a) BM3D, (b) KUAN, (c) LEE, (d) NLLR, (e) PPB, and (f) proposed methods.
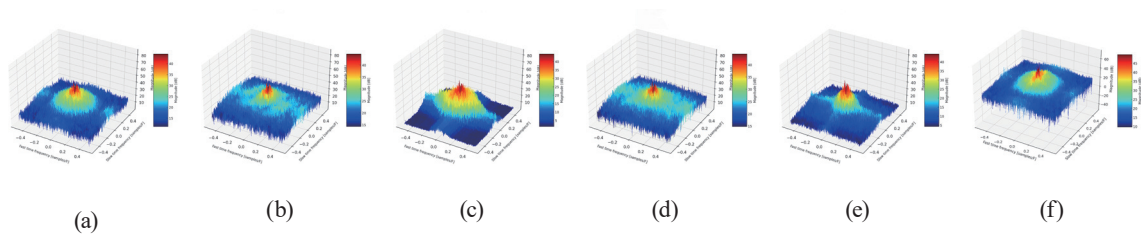

(a)　　　　(b)　　　　(c)　　　　(d)　　　　(e)　　　　(f)

Fig. 7. (Color online) PSD modeling of despeckling results in road image under (a) BM3D, (b) KUAN, (c) LEE, (d) NLLR, (e) PPB, and (f) proposed methods.

Table 2
PSD modeling results after speckle noise suppression.

Images	Methods					
	BM3D (dB)	KUAN (dB)	LEE (dB)	NLLR (dB)	PPB (dB)	Proposed (dB)
Building	17.49	21.53	22.61	21.15	21.33	13
Road	21.51	19.04	13.78	22.06	4.80	9

the KUAN method shown in Figs. 5(b) and 7(b) shows a slightly broader peak, indicating less focused noise reduction. The LEE method shown in Fig. 7(c) exhibits a wider spread of the peak values, indicating that there is still some presence of speckle noise. Although the PSD peak value of the proposed method in Table 2 is not as low as that of the PPB method, the peak value of this method is scattered, as shown in Fig. 7(e), indicating that the overall board reduction effect is not significant. In short, the proposed method illustrated a notable reduction and concentration in the PSD peak magnitude, indicating superior noise suppression.

The further quantitative metrics of the building and road images for different despeckling methods are shown in Table 3. Through comparative analysis, it is observed that under the BM3D, KUAN, LEE, PPB, and NLLR methods, the PSNR value of the image after despeckling is lower than 30. This means that the despeckling quality is not good. In contrast, the PSNR value after the proposed algorithm despeckling is higher than 30, which is larger than those of the other despeckling methods. Additionally, the proposed algorithm achieved the lowest MAE value for this despeckling image. In comparison with the other methods, the proposed method yielded a despeckling image with an SSIM value approaching 1, and the ENL value showed that the spot reduction ability of our algorithm is stronger than those of the other five algorithms. Finally, although the CPU time is not the shortest in some cases, the significant improvement in denoising quality indicates its potential for image processing. The six indicators from Table 3 unequivocally demonstrate the unparalleled superiority of the proposed noise reduction method over other existing techniques. Consequently, on the basis of our meticulous analysis, it can be deduced that the proposed technique surpasses all previous state-of-the-art methodologies.

3.2   Practical experiment and result analysis

To demonstrate the effectiveness of speckle noise reduction on a real SAR image, Sentinel -1A, a type of SAR data, from Beijing, China, in 2018 with a size of 816 × 750 is collected, as shown in Fig. 8. This type of satellite SAR image showed a sufficient presence of speckle, making it an optimal choice for conducting an experiment simulating real-world noisy SAR data. Figure 8 also shows the reference SAR image sample and the resulting PSD function modeling. Table 4 shows the PSD results based on the peak values of the real-world SAR image.

As with the algorithm steps in previous section, the experimental parameters of this compared techniques are fine-tuned to achieve the most favorable outcome. The SAR image despeckling effects under six different methods are shown in Figs. 9 and 11. The corresponding PSD outcomes are depicted in Figs. 10 and 12, and the PSD values are shown in Table 5. The quantitative quality evaluation indicators of the field and park images for different despeckling methods are shown in Table 6.

Upon visual inspection of Figs. 9 and 11, it is evident that the image after despeckling by the proposed algorithm is similar to the original image. Specifically, the BM3D method depicted in Fig. 11(a) preserved the details of the park's lake, but these details of its structure are not retained. KUAN, LEE, PPB, and NLLR depicted in Figs. 9 and 11 also exhibit indications of excessive smoothing. On the other hand, the proposed algorithm successfully maintained most of the finer details while generating a noise-free image. Careful observation showed that the proposed technique demonstrates superior despeckling capabilities.

Table 3
Despeckling results obtained using different methods.

Images	Methods	Parameters					
		PSNR	SSIM	MAE	ENL	EPI	CPU time
Building	BM3D	20.88	0.899	122.52	0.91	1.52	2.3214
	KUAN	21.94	0.900	121.21	0.98	1.52	1.2854
	LEE	22.34	0.902	120.35	0.95	1.52	14.2633
	NLLR	23.56	0.887	122.34	0.94	1.68	2.0214
	PPB	22.95	0.903	121.34	0.95	1.68	2.2157
	Proposed	30.52	0.965	114.87	0.99	1.70	1.9655
Road	BM3D	13.21	0.826	128.62	0.80	0.75	2.5835
	KUAN	14.27	0.801	131.02	0.79	0.87	1.2452
	LEE	13.98	0.795	128.97	0.72	0.91	4.7462
	NLLR	12.52	0.820	128.32	0.90	0.97	3.2418
	PPB	11.02	0.810	128.64	0.81	0.91	7.5414
	Proposed	30.01	0.862	124.21	1.07	0.94	2.2475

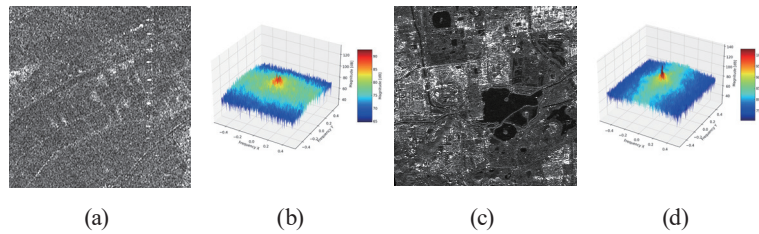

(a)　　　　　(b)　　　　　(c)　　　　　(d)

Fig. 8.　(Color online) Real-world SAR images used in practical experiment [(a) field and (c) park] and the PSD modeling of the real-world SAR images [(b) PSD of field and (d) PSD of park].

Table 4
PSD modeling results before speckle noise suppression.

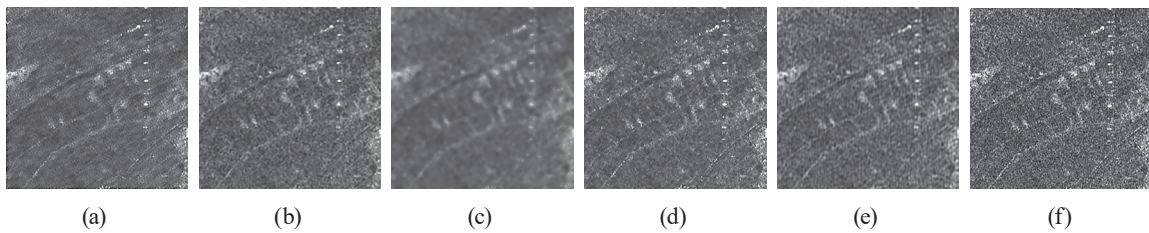| Images	Values (dB)
Field	62
Park	56

(a)　　　　　(b)　　　　　(c)　　　　　(d)　　　　　(e)　　　　　(f)

Fig. 9.　Despeckling results in field image using (a) BM3D, (b) KUAN, (c) LEE, (d) NLLR, (e) PPB, and (f) proposed methods.

The PSD distributions of the field and park images before and after speckle noise reduction are shown in Figs. 10 and 12, respectively. The despeckling PSD values for authentic SAR images are presented in Table 6. The peak values of these result after BM3D, KUAN, and LEE
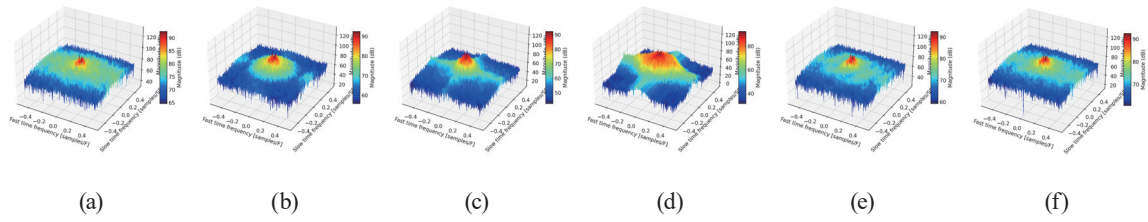
Fig. 10. (Color online) PSD modeling of despeckling results in field image under (a) BM3D, (b) KUAN, (c) LEE, (d) NLLR, (e) PPB, and (f) proposed methods.
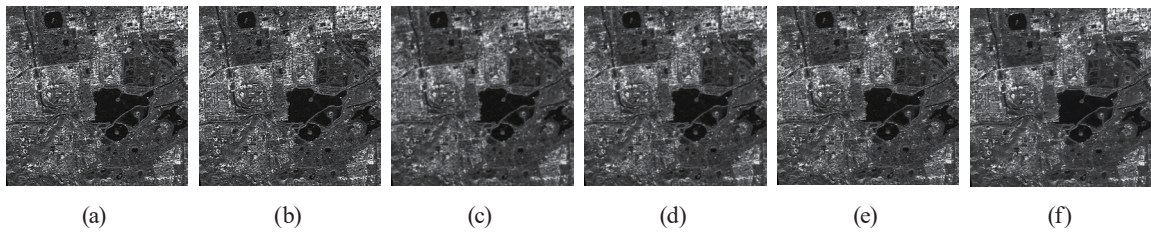

Fig. 11. Despeckling results in park image using (a) BM3D, (b) KUAN, (c) LEE, (d) NLLR, (e) PPB, and (f) proposed methods.
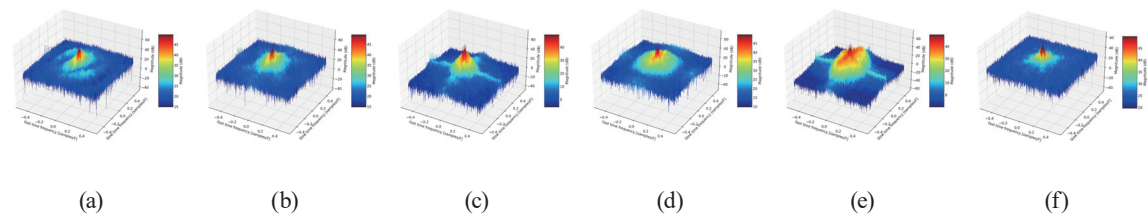

Fig. 12. (Color online) PSD modeling of despeckling results in park image under (a) BM3D, (b) KUAN, (c) LEE, (d) NLLR, (e) PPB, and (f) proposed methods.

Table 5
PSD modeling results after speckle noise suppression.

Images	Methods					
	BM3D (dB)	KUAN (dB)	LEE (dB)	NLLR (dB)	PPB (dB)	Proposed (dB)
Field	43	39	33	55	51	32
Park	35	33	32	45	49	28

processing are significantly reduced, and the low-frequency regions are also smooth as a whole. It can be seen that these methods have a certain effect on the speckle removal of real SAR images, but the edges and details are also easily blurred. After processing by the proposed method shown in Figs. 9(f) and 11(f), the peak values of PSD results are removed, and the change in frequency value in the low-frequency region is not significant. It can be seen that these algorithms retain certain detailed information about SAR images while reducing speckle noise.

Table 6
Despeckling results obtained using different methods.

Images	Methods	Parameters					
		SSIM	CV	MoR	EPI	ENL	CPU time
Field	BM3D	0.910	0.22	0.29	1.70	1.004	5.6235
	KUAN	0.933	0.11	0.29	1.34	1.010	8.5545
	LEE	0.901	0.11	0.40	1.54	1.007	10.8120
	NLLR	0.900	0.15	0.37	1.42	1.007	4.5274
	PPB	0.900	0.17	0.30	1.50	1.005	6.5201
	Proposed	0.944	0.23	0.42	1.73	1.044	4.8542
Park	BM3D	0.801	0.20	0.22	1.50	0.980	6.5689
	KUAN	0.692	0.30	0.20	1.20	0.899	5.3621
	LEE	0.600	0.20	0.31	1.12	1.000	10.3569
	NLLR	0.713	0.11	0.28	1.62	1.001	6.0047
	PPB	0.700	0.34	0.23	1.68	1.001	4.8550
	Proposed	0.811	0.37	0.35	1.90	1.111	4.5048

To validate the proposed algorithm's effectiveness, CV and MoR are used to determine texture and radiometric information preservation.[32] The performance characteristics of the proposed method as shown in Fig. 9(f) and Fig. 11(f) are found to be comparable in terms of CV and MoR. The LEE and KUAN methods reported lower ENL values and higher CV and SSIM values than the PPB method. BM3D outperformed other methods in terms of MoR across all images but had slightly lower ENL values than the other methods. The proposed method demonstrated superior performance measures compared with the other methods in terms of the field and park images. In comparison with PPB, the proposed method exhibited competitive ENL, CV, and SSIM values for the park image owing to its effective noise smoothing capability. However, note that while PPB achieved high noise reduction, it compromised detail preservation such as texture and radiometry resulting in a lower MoR value than that of our proposed method. Additionally, the proposed approach had a shorter CPU time in real SAR images. This feature will become a significant advantage when processing SAR images in batches. Thus, the proposed method yielded the most favorable outcome among all approaches.

4. Conclusions

The interpretation of SAR images is always affected by speckle noise. Aiming to enhance the effectiveness of SAR image despeckling, we propose an innovative method that combines IVA and an improved FastICA. The method can minimize excessive smoothing and distortion during image noise reduction. It can also preserve the correlations between different SAR data sources. The proposed method is compared with existing methods and has shown exceptional performance in reducing speckle noise through both simulated and practical experiments. The following conclusions are obtained.
(1) In the simulation experiment, the proposed method shows excellent performance on multiple quantitative indexes. For instance, the PSNR index is improved by about 8.48% and the SSIM index is about 6.92% higher than the other methods. Thus, the proposed method is better than the other methods.

(2) The practical experiment also yields the most favorable outcome among all approaches, especially in CV with an increase of about 74.99%. Moreover, it shows certain CPU time reduction. A faster CPU time can significantly enhance overall efficiency for large-scale data batch processing.

The proposed method shows significant despeckling capabilities in both simulations and practical experiments. However, its effectiveness is somewhat limited in urban environments with dense skyscrapers and mountainous regions with complex topography. Furthermore, signal attenuation worsened by extreme weather conditions, particularly in high-frequency bands. This highlights the need for further research in these specific scenarios. Additionally, while the method enhances convergence speed and stability and reduces its reliance on initial values, using random initial values does not meet the requirement for high iteration accuracy. Future research will therefore aim to refine the selection of initial values to mitigate image distortion, ensuring a more cohesive approach to addressing these challenges.

Acknowledgments

References

1 H. Cruz, M. Véstias, J. Monteiro, H. Neto, and R. P. Duarte: Remote Sens. **14** (2022) 1258. https://doi.org/10.3390/rs14051258

2 S. W. Paek, S. Balasubramanian, S. Kim, and O. de Weck: Remote Sens. **12** (2020) 2546. http://doi.org/10.3390/rs12162546

3 G. Xu, B. Zhang, H. Yu, J. Chen, M. Xing, and W. Hong: IEEE Geosci. Remote Sens. Mag. **10** (2022) 32. http://doi.org/10.1109/MGRS.2022.3218801

4 R. J. Soldin: Applied Imagery Pattern Recognition Workshop (AIPR) (2018) 1. http://doi.org/10.1109/AIPR.2018.8707419

5 I. K. Lee, A. Shamsoddini, X. Li, J. C. Trinder, and Z. Li: ISPRS J. Photogramm. Remote Sens. **117** (2016) 115. http://doi.org/10.1016/j.isprsjprs.2016.03.020

6 M. Afonso and J. M. Sanches: Neurocomput. **150** (2015) 200. https://doi.org/10.1016/j.neucom.2014.08.073

7 D. Devapal, S. Kumar, and C. Jojy: J. Indian Soc. Remote Sens. **45** (2017) 443. https://doi.org/10.1007/s12524-016-0607-0

8 M. E. Salih, X. Zhang, and M. Ding: Open Access Libr. J. **9** (2022) 1. https://doi.org/10.4236/oalib.1108618

9 F. Gao, X. Xue, J. Sun, J. Wang, and Y. Zhang: IEEE Trans. Geosci. Remote Sens. **54** (2016) 3025. https://doi.org/10.1109/TGRS.2015.2510161

10 H. Chen, J. Huang, O. Remil, H. Xie, J. Qin, Y. Guo, M. Wei, and J. Wang: Comput.-Aided Des. **115** (2019) 122. https://doi.org/10.1016/j.cad.2019.05.036

11 S. Liu, M. Liu, P. Li, J. Zhao, Z. Zhu, and X. Wang: IEEE Trans. Geosci. Remote Sens. **55** (2017) 2985. https://doi.org/10.1109/TGRS.2017.2657602

12 W. Wang: China Commun. **4** (2016) 126. https://doi.org/10.1109/CC.2016.7559084

13   Y. Zhang and D. Zhu: IEEE Sens. J. **18** (2018) 8108. https://doi.org/10.1109/JSEN.2018.2865112

14   M. Kalaiyarasi, S. Saravanan, and B. Perumal: Int. Conf. Control, Instrumentation, Communication and Computational Technologies (ICCICCT) (2016) 54. http://doi.org/10.1109/ICCICCT.2016.7987919

15   S. Wei, H. Zhang, C. Wang, Y. Wang, and L. Xu: Remote Sens. **11** (2019) 68. https://doi.org/10.3390/rs11010068

16   A. Tharwat: ACI. **17** (2021) 222. https://doi.org/10.1016/j.aci.2018.08.006

17   S. Bhinge, Z. Boukouvalas, Y. Levin-Schwartz, and T. Adali: IEEE Int. Conf. Acoustics, Speech and Signal Processing (ICASSP) (2016) 2494. http://doi.org/10.1109/ICASSP.2016.7472126

18   I. Heidarpour Shahrezaei and H.-c. Kim: Remote Sens. **11** (2019) 1041. https://doi.org/10.3390/rs11091041

19   O. Frey and E. Meier: IEEE Trans. Geosci. Remote Sens. **49** (2011) 3648. https://doi.org/10.1109/TGRS.2011.2125972

20   T. Adali, M. Anderson, and G.-S. Fu: IEEE Signal Process Mag. **31** (2014) 18. https://doi.org/10.1109/MSP.2014.2300511

21   M. Anderson, X.-L. Li, and T. Adalı: Signal Process. **92** (2012) 1821. https://doi.org/10.1016/j.sigpro.2011.09.034

22   M. Anderson, G.-S. Fu, R. Phlypo, and T. Adalı: IEEE Trans. Signal Process. **62** (2014) 4399. https://doi.org/10.1109/TSP.2014.2333554

23   Z. Koldovský and P. Tichavský: IEEE Trans. Signal Process. **67** (2018) 1050. https://doi.org/10.1109/TSP.2018.2887185

24   T. Adalı: Sens. Anal. Technol. Biomed. Cognit. Appl. **9871** (2016) 182. https://doi.org/10.1117/12.2244119

25   Z. Luo: Pattern Recognit. **138** (2023) 109376. https://doi.org/10.1016/j.patcog.2023.109376

26   T. Adali, Y. Levin-Schwartz, and V. D. Calhoun: Proc. IEEE **103** (2015) 1478. https://doi.org/10.1109/JPROC.2015.2461624

27   S. Gou, X. Zhuang, H. Zhu, and T. Yu: IEEE J. Sel. Top. Appl. Earth Obs. Remote Sens. **6** (2013) 1949. https://doi.org/10.1109/JPROC.2015.2461601

28   H. Y. Li, M. Ye, and D. Zhao: Appl. Mech. Mater. **411** (2013) 1125. https://doi.org/10.1109/JSTARS.2012.2230435

29   J. Peng, A. Liao, Z. Peng, and Z. Chen: Linear Multilinear Algebra **67** (2019) 1867. https://doi.org/10.1080/03081087.2018.1472736

30   C.-H. Guo, W.-W. Lin, and C.-S. Liu: Numerical Algorithms **80** (2019) 595. https://doi.org/10.1007/s11075-018-0498-y

31   M. N. Khan and A. Altalbe: Biomed. Signal Process. Control. **73** (2022) 103399. https://doi.org/10.1016/j.bspc.2021.103399

32   F. Guo, C. Sun, N. Sun, X. Ma, and W. Liu: Remote Sens. **15** (2023) 1409. https://doi.org/10.3390/rs15051409

33   S. n. laboratories: https://www.sandia.gov/radar/?page_id=129 (02 October 2020).

34   S. G. Dellepiane and E. Angiati: IEEE J. Sel. Top. Appl. Earth Obs. Remote Sens. **7** (2013) 691. https://doi.org/10.1109/JSTARS.2013.2279501